Effect of Boron Addition on Creep Strain during Impression Creep of P91 Steel

Akhil Khajuria, Rajneesh Kumar, and Raman Bedi

In an attempt to understand the effect of boron addition on creep deformation behavior under high stress and high temperature in martensitic P91 steel, impression creep tests were carried out on boron-free P91 (P91) and boron-added P91 (P91B) steels. The experimental program consisted of three steps, i.e., characterization of as-received steels by microhardness, optical microscopy (OM), transmission electron microscopy (TEM), electron backscattered diffraction (EBSD) and wavelength-dispersive spectroscopy (WDS); impression creep tests at 445 MPa and 625 °C on as-received steels; characterization at deformed plastic zones of impression-crept specimens by microhardness, OM, EBSD, TEM and WDS. Impression creep tests were run till a depth of penetration of 1.8 mm was achieved for both cases which ensured a sufficient plastic zone underneath indenter for subsequent microstructural investigations. Coarsening of $M_{23}C_6$ carbides was observed in P91 steel during high-temperature creep loading, which leads to extensive strain hardening in deformed plastic region, resulting in impaired creep performance. On the contrary, dynamic recrystallization in P91B steel results in formation of small strain-free grains during creep loading which are responsible for increased resistance of the material to shear stresses during an impression creep test.

1. Introduction

There has been an intense effort across the world to develop new generation ferritic/martensitic steels which can sustain harsh thermo-mechanical conditions in power generation units. The demand for improvements in the efficiency of thermal power plants is strongly linked to reduce CO_2 emissions, in order to meet environmental obligations (Ref 1). P91 steel (9Cr1Mo) is ferritic/martensitic steel and was originally developed by Oak Ridge National Laboratory (ORNL), USA, in 1970s, for fast breeder reactors (Ref 2). Later, this steel was modified with the addition of Nb, V for pressure vessels to fulfill enhanced creep resistance requirement to cope with higher working steam temperatures and pressures. Fusion welding of P91 is an unavoidable practice for fabrication of thick-walled components like boiler headers, superheater tubes, etc., in power plant industry. The high heat input of fusion welding significantly influences microstructural evolution across the P91 weldment and introduces metallurgical notch at heat-affected zone resulting in high triaxiality which promotes cavitation at higher service temperatures (Ref 3).

Such cavities coalesce to form creep voids over a due course of service exposure and thus the weldment ruptures by a phenomenon referred to as type IV cracking (Ref 4). The addition of controlled boron (90-130 ppm) with low levels of nitrogen to modified P91 steel seems to provide an alternative for providing uniformity in mechanical properties and creep strength enhancement in base alloys and their weldments (Ref 5-8). However, the mechanisms pertaining to improvements in creep performance and mitigation of type IV cracking are still being investigated. Conventional tensile creep testing requires a substantial amount of material and time. One method which is receiving attention is a modified form of indentation test termed as impression creep test. This test uses a small amount of material with less time to screen out creep properties under constant loading (Ref 9, 10). In an impression creep test, material is deformed locally which produces three distinguishable zones beneath the indenter. These are zone of hydrostatic stress with no deformation, hemispherical deformed plastic zone with wide shear deformation being dominant at edges of impression and unaffected zone with no plastic deformation (Ref 11-13). Creep resistance of P91 alloy is sensitive to microalloying elements, recovery of martensite, heat treatments, precipitate size and shape present in this grade which significantly affects the microstructural evolution during creep (Ref 14-20). For boron-added P91 steel, it is inferred that soluble boron retards coarsening of $M_{23}C_6$ at grain boundaries and imparts grain and subgrain boundary hardening during creep exposure (Ref 21). In an effort to investigate the effect of boron in improving the creep performance of P91 steels and mitigating type IV cracking, an extensive investigation is being currently underway. The results presented in this paper are a part of that investigation and aim to study the microstructural features of the deformed/crept zone of P91 and P91B in an endeavour to understand the fundamental role of boron in providing the enhanced creep performance in boron-added P91 steel.

Akhil Khajuria and **Raman Bedi**, Department of Mechanical Engineering, Dr. B R Ambedkar National Institute of Technology, Jalandhar, Punjab 144011, India; and **Rajneesh Kumar**, Project Planning and Engineering Division, CSIR-National Metallurgical Laboratory, Jamshedpur, Jharkand 831007, India. Contact e-mail: rkgupta@nmlindia.org.

2. Experimental Program

2.1 As-Received Steels

P91 and P91B steels processed with normalizing temperature of 1050 °C for 30 min and tempered at 760 °C for 2 h were used in this work. Chemical compositions for both grades as determined by direct reading spectrograph (DRS) method and inductively coupled plasma–optical emission spectrometer (ICP-OES) method for small elements like boron, carbon, nitrogen, etc., are shown in Table 1. It should be noted that P91 contains 22 ppm of boron as detected by chemical analysis. However, such small percentage is not sufficient to show any effect on creep resistance of steel alloy P91. Therefore, it is referred to as boron-free P91 steel in subsequent analysis in this work.

2.2 Impression Creep Tests and Microstructure Studies

Impression creep test has been developed with a main motive to reduce the time taken in a conventional creep tests. The prime motive of this investigation was to qualitatively compare creep resistance of selected steels due to variation in boron alloying. Impression creep testing has been conducted to understand deformation resistance and effect of exposure on microstructure of both the steels. Yu and Li found conversion factor of 3.3 from finite element approach in order to equalize stress levels between unidirectional tensile and impression creep techniques which is applicable for most of the materials (Ref 22). Therefore, for present study, impression creep tests were carried out at 625 °C and a punching stress of 445 MPa corresponding to uniaxial creep stress of 135 MPa. Load equivalent to a punching stress (σ_{imp}) of 445 MPa is determined by equation $\sigma_{imp} = \frac{4F}{\pi D^2}$ where F is the compressive load on the sample and D is the diameter of indenter, whereas creep rate arising in time t due to penetration depth h is calculated by dividing instantaneous strain by time. To develop correlation among uniaxial creep and impression creep, equations $\sigma_{uni} = \alpha\sigma_{imp}$ and $\dot{\varepsilon}_{uni} = \frac{V_{imp}}{\beta D}$ have been used by various researchers (Ref 23-30) where σ_{uni} and $\dot{\varepsilon}_{uni}$ are uniaxial stress and steady state strain rate, V_{imp} is change in indenter penetration depth corresponding to a time interval, and α and β are correlation factors and have values in the range 0.26-0.33 and 1, respectively. Development of a correlation between uniaxial and impression creep for P91 and P91B steel requires data of minimum creep rate (MCR) obtained from uniaxial and impression creep tests at 625 °C and a minimum of four stress levels.

Tungsten carbide indenter with diameter of 2 mm was used for conducting impression creep tests on both P91 and P91B steel samples with dimensions 10 mm × 10 mm × 10 mm. The purpose of using indenter of bigger diameter was to ensure sufficient localized deformation so that further microstructural evolution could be investigated underneath the indenter for both steels. The vacuum chamber was maintained at a pressure of 10^{-6} mbar during the creep test with the help of high vacuum system in order to avoid atmospheric oxidation.

As it was planned in this investigation to study the fundamental effect of boron addition in P91 steel on its creep performance through various manifestations in the form of microstructural inhomogeneities like size and shape of prior austenite grain boundaries (PAGB), size and distribution of precipitates, distribution of microalloying elements, etc., microstructural studies were necessary (Ref 31-35). Samples for optical microscopy and microhardness were prepared by standard polishing techniques. Microstructures of as-received steels were revealed by etching with Nital (solution of 28 ml nitric acid + 100 ml ethanol). Grain size calculations were done by linear intercept method. For analysis of deformed microstructure formed beneath the indenter after an impression creep test, the crept sample was cut by wire EDM, 1 mm away from impressed area. Further, segmented surface was carefully polished by SiC paper so that the final finished surface passed through the center of impression. Vickers hardness for as-received steel was taken at 500 g load and 10 s dwell time on Leica VMHT autotester. To examine variation in hardness after impression creep test in the localized deformed and undeformed regions, indentations were taken at the same load and dwell time. For estimating precipitate size, 3-mm-diameter circular and 80-μm-thin disks from as-received steels were twin-jet-polished by 10% perchloric acid and 90% ethanol electrolyte and were examined in JEOL 2200FS TEM at an accelerating voltage of 200 kV. To know the distribution of major alloying elements in as-received steels and deformed regions of crept P91 and P91B samples, wavelength-dispersive spectroscopy (WDS) area scans were taken on electron probe microanalyzer of model JEOL-JXA-8230. For characterizing as-received steels and microstructural evolution in the most deformed zone of crept steel samples, electron backscattered diffraction (EBSD) scans were taken for both grades at a step size of 0.2 μm. For this purpose, samples were electropolished with a solution of 80 ml methanol and 20 ml perchloric acid. EBSD data analysis was done on TSL-OIM 7 software.

3. Results and Discussion

3.1 Microstructural Characterization of AR-P91 and AR-P91B Steels

3.1.1 Optical Microscopy and TEM Analysis. Microstructures of as-received P91 and P91B steels show tempered martensitic structure as shown in Fig. 1(a) and (b). Primary aim of tempering was to relieve residual stresses produced after normalizing, but due to different nucleation temperatures of carbides, this tempering also results in coarsening of large number of pre-existing carbides in the overall structure as revealed by Nital for both alloys. P91B steel

Table 1 P91 and P91B chemical compositions in wt.%

| Element	C	Cr	Mo	Si	Mn	V	Nb	Ni	Al	N	B	Ti	Fe
P91	0.11	9.44	0.71	0.21	0.3	0.2	0.05	0.223	…	0.06	0.0022	…	Bal.
P91B	0.10	8.26	0.88	0.3	0.33	0.186	0.06	0.01	0.03	0.004	0.01	0.0041	Bal.
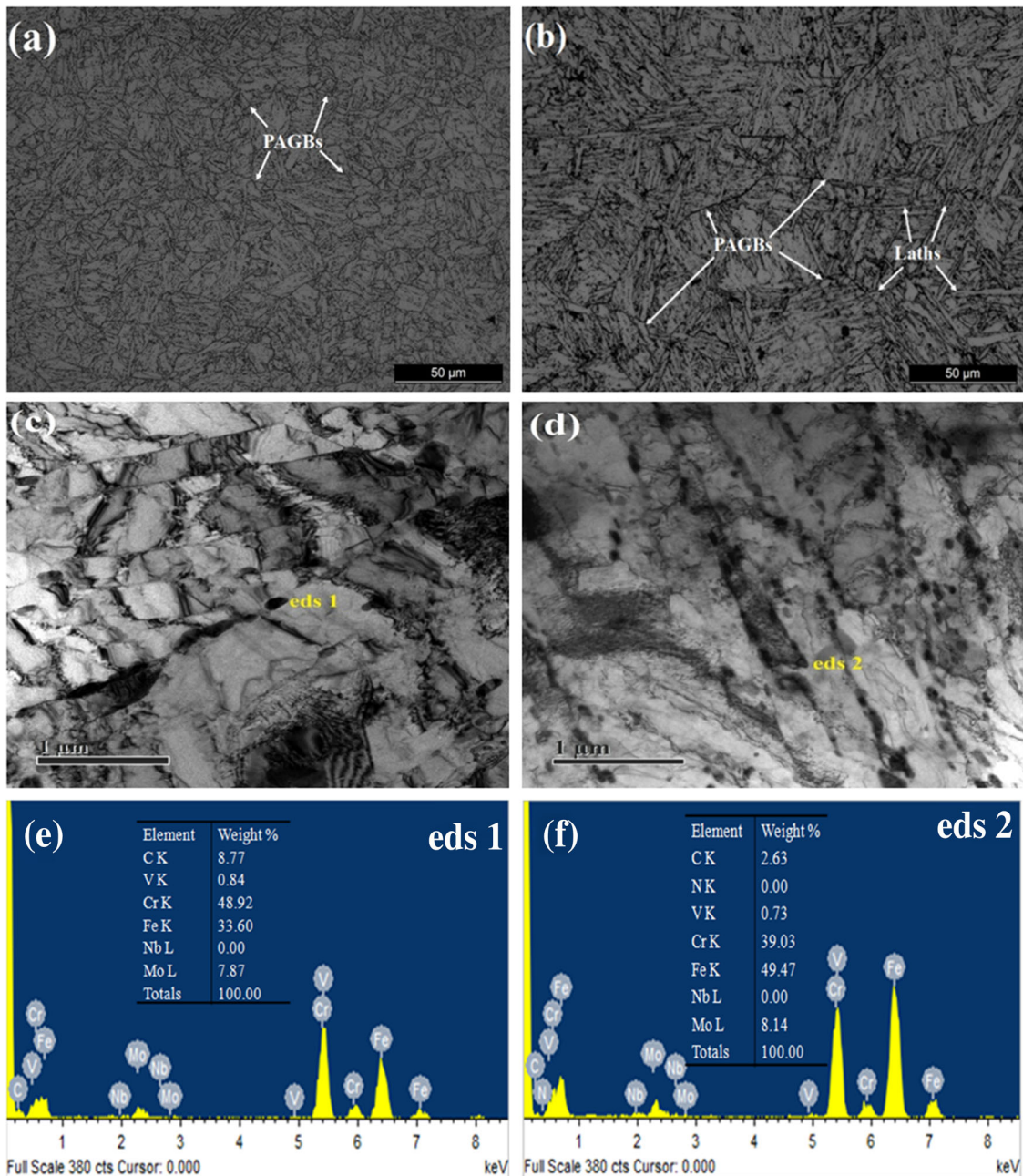
Fig. 1 Microstructures of (a) optical-P91, (c) bright-field TEM-P91, (e) spot EDS-P91, (b) optical-P91B, (d) bright-field TEM-P91B and (f) spot EDS-P91B normalized at 1050 °C/30 min and tempered at 760 °C/2 h

exhibits large prior austenite grain (PAG) size with acicular morphology which is of the tune 28 μm as compared to P91 where comparatively small grains with polygonal morphology with an average PAG size of 18 μm are present. A probable reason can be the addition of boron, which impedes cellular grain boundary construction in high chromium heat resistant alloys (Ref 36). It is reasonable to mention here that an increase in PAG size indicates an increase in size of PAG packets and martensite lath blocks in P91B. Non-uniformity in PAG distribution is seen for both the steels. PAGs are observed with varying size and amount of carbides inside the grains. Martensite laths taking a needle-like form appear dominant in P91B with relatively less inter-lath spacing in contrast to P91.

Figure 1(c) and (d) shows high magnification images of both alloys captured in bright-field TEM mode where relatively coarse carbides of $M_{23}C_6$ (M = Fe, Cr, V, Mo) type are observed on lath boundaries in P91 as compared to P91B. Thermodynamically, $M_{23}C_6$ particles are most stable form of carbides in P91 steel and exist in round as well as acicular shapes (Ref 37). Large regions devoid of these carbides are observed in P91, whereas small regions are present in P91B with fairly uniform distribution of fine carbides along lath boundaries. Fine carbides along lath/grain boundaries help in assisting effective bonding area in between PAGs and among laths which further improve pinning of carbides. The average $M_{23}C_6$ carbide size in P91B is in the range of 50-310 nm,
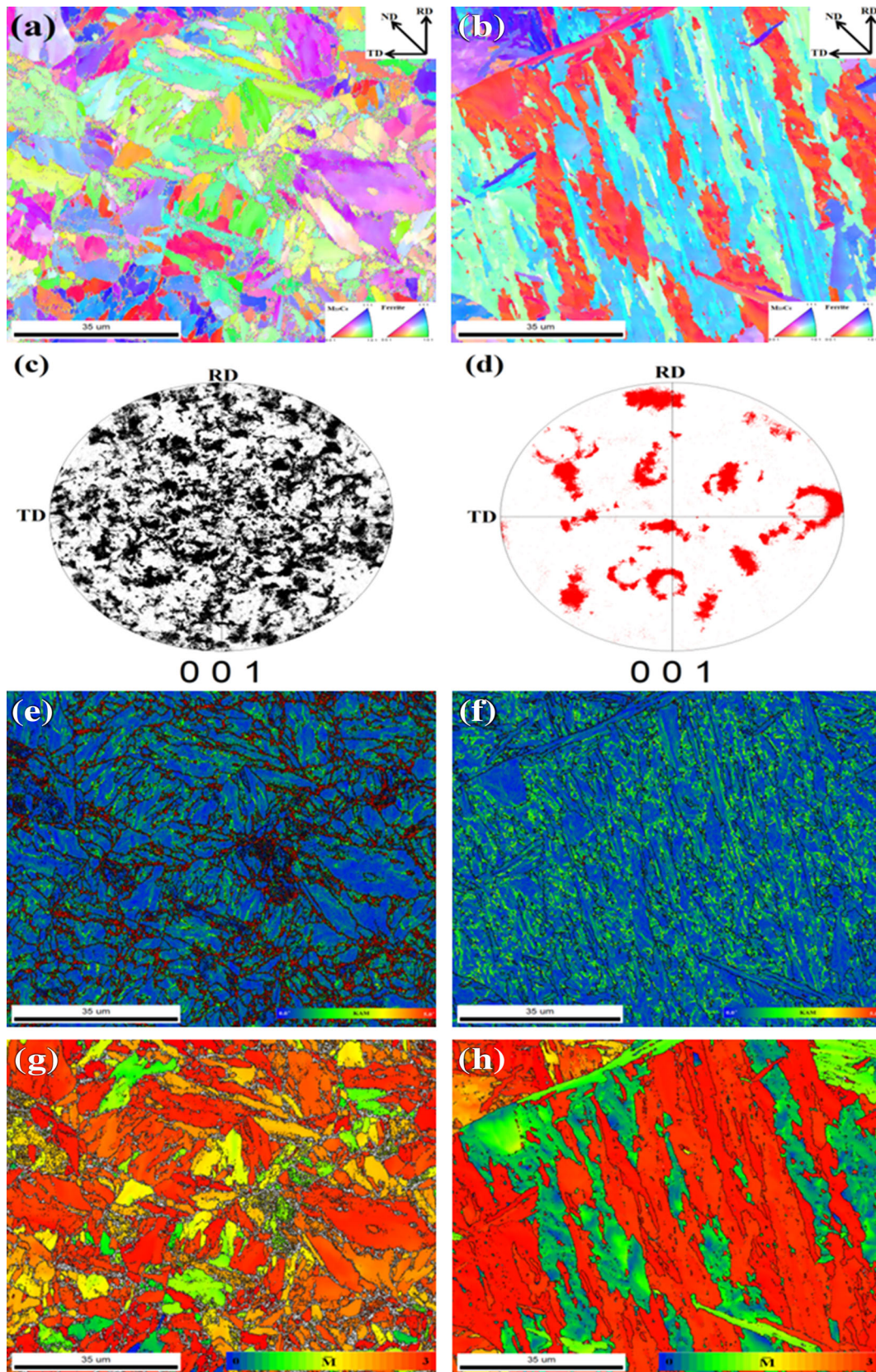
Fig. 2 EBSD color-coded maps and pole figures of as-received steels (a) P91-IPF map with grain boundaries, (c) P91-pole figure, (e) P91-KAM map, (g) P91-Taylor factor, (b) P91B-IPF map with grain boundaries, (d) P91B-pole figure, (f) P91B-KAM map and (h) P91B-Taylor factor (Color figure online)
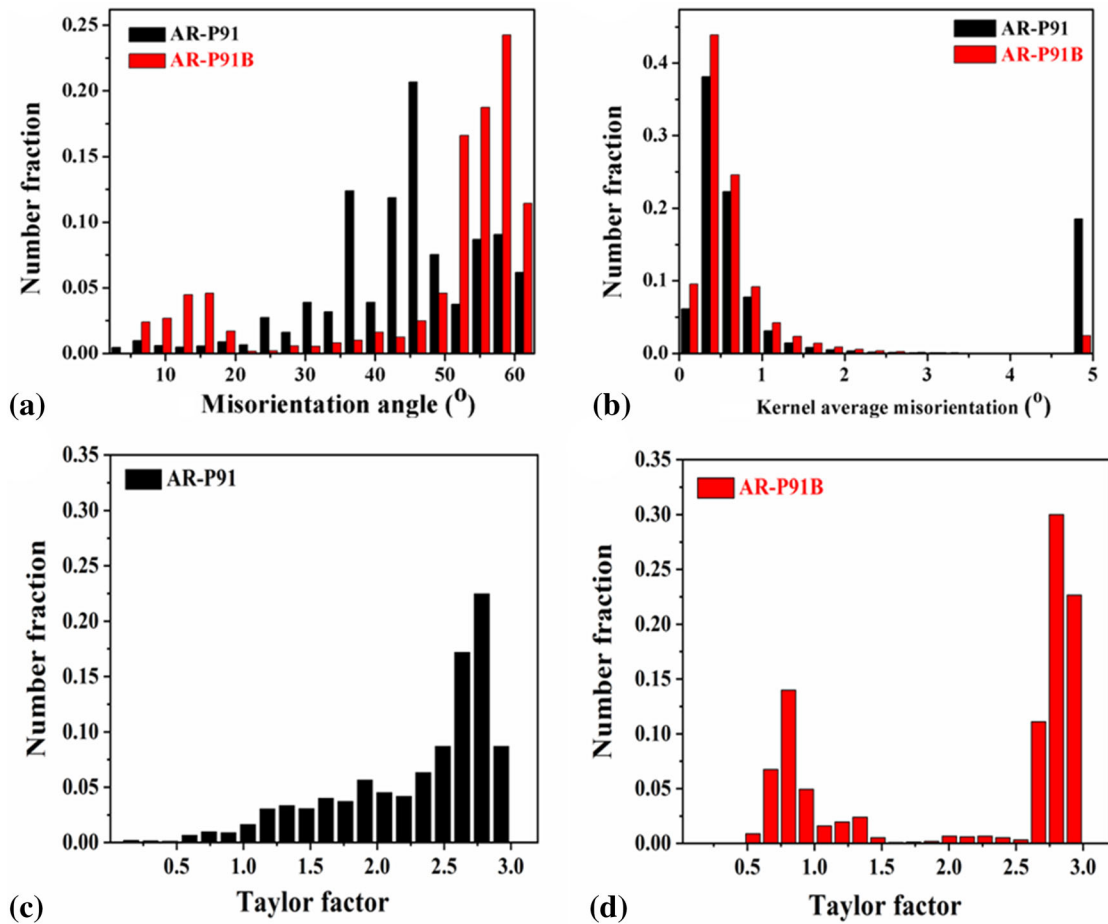
Fig. 3 EBSD analysis of as-received steels (a) misorientation angle chart-P91 and P91B, (b) KAM chart-P91 and P91B, (c) P91-Taylor factor chart and (d) P91B-Taylor factor chart

whereas for P91 it is 85-630 nm. Spot EDS shown in Fig. 1(e) and (f) confirms presence of $M_{23}C_6$ carbides in both steel grades.

3.1.2 EBSD and WDS Analysis. Grain orientation is revealed by a color-coded figure called as inverse pole figure (IPF) map. The IPF maps of AR-P91 and AR-P91B steels are shown in Fig. 2(a) and (b). The area of IPF map with identical color specifies identical orientation of martensite laths. Since the step size during scanning was kept 0.2 μm with ferrite and $M_{23}C_6$ as phases, therefore carbides and martensitic laths less than 200 nm could not be indexed by EBSD. IPF maps show that $M_{23}C_6$ carbides are dominant at PAGBs and block boundaries in P91, whereas grains are stacked on each other in P91B. Pole figures in Fig. 2(c) and (d) indicate that grains are randomly oriented in P91 as regards P91B. The density of $M_{23}C_6$ carbides is high in few blocks, rest being completely empty in P91. On the contrary, a small number of $M_{23}C_6$ carbides were indexed in P91B on lath boundaries inferring their fewer fractions in higher-order size. The MX type of carbonitrides could not be revealed by EBSD due to their extremely small size of order 5-20 nm (Ref 38). Furthermore, lengthy and coarse martensite lath blocks are observed in IPF map of P91B in contrast to P91 where short and relatively fine lath blocks are observed. The statistical results obtained from TSL-OIM software for EBSD analysis are presented in the form of charts as shown in Fig. 3 for as-received P91 and P91B

steels. Orientations of martensite laths in creep-resistant steels play a vital part in controlling the metal properties at elevated temperatures and stresses since they obstruct the dislocation motion and directly influence the grain boundary energy. A grain boundary is distinguished among neighboring grains having different orientations and is measured in terms of misorientation angle (Θ). Small misorientation angles in the tune of $\Theta \sim 2°$ to $10°$ are low-angle grain boundaries (LAGB), whereas large misorientation angles when $\Theta > 10°$ are high-angle grain boundaries (HAGB). For measuring the fraction of martensite lath boundaries and PAGBs, $\Theta > 50°$ and $\Theta \sim 20°$ to $50°$ for 9Cr steels with common axis ⟨110⟩, respectively (Ref 39, 40). Figure 3(a) gives the comparison of number fraction distribution of grain boundaries based on measured misorientation angles in as-received steels. It may be pointed out that fraction of martensite lath boundaries is quite larger in boron-added P91, whereas the fraction for PAGBs is greater in boron-free P91. This implies that big laths exist in P91B with relatively large PAGs than P91 which is also confirmed by optical micrographs of both alloys.

The local strain distribution in the microstructure is calculated by kernel average misorientation (KAM). It shows the distribution of local misorientation based on a kernel average misorientation of the grain to which the point belongs. Color variation in KAM map shown in Fig. 2(e) and (f) indicates non-homogenous distribution of local strain across the
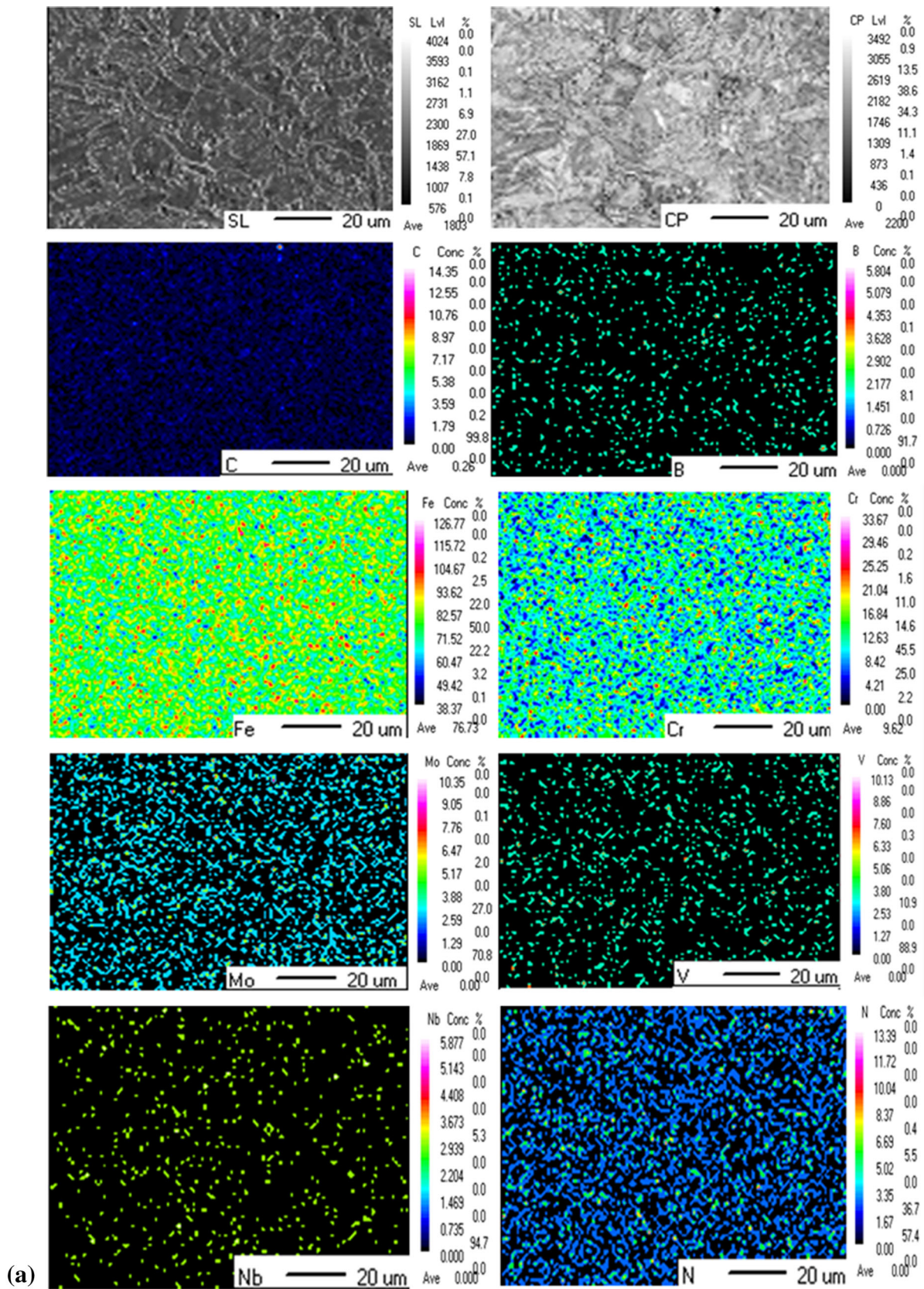
Fig. 4 Elemental mapping of as-received steels (a) P91 and (b) P91B
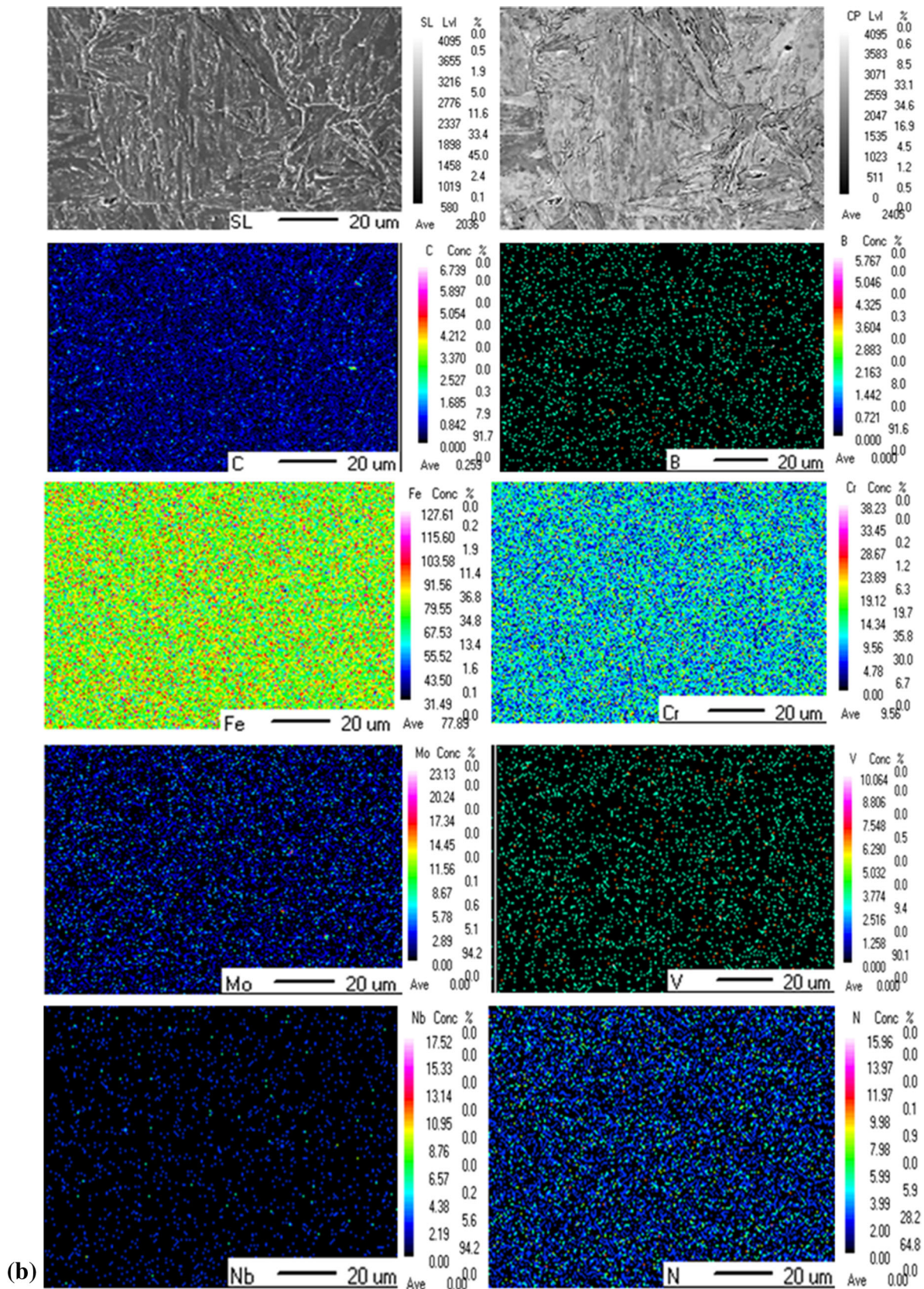
Fig. 4 continued

microstructure of as-received P91 and P91B steels. Higher strain values are observed at PAGBs of P91, which can be attributed to larger size of carbides present on grain boundaries as these are responsible for increased localized strain. The same results in higher average KAM value in P91 as compared to P91B where fine carbides reduce strain accumulation at grain
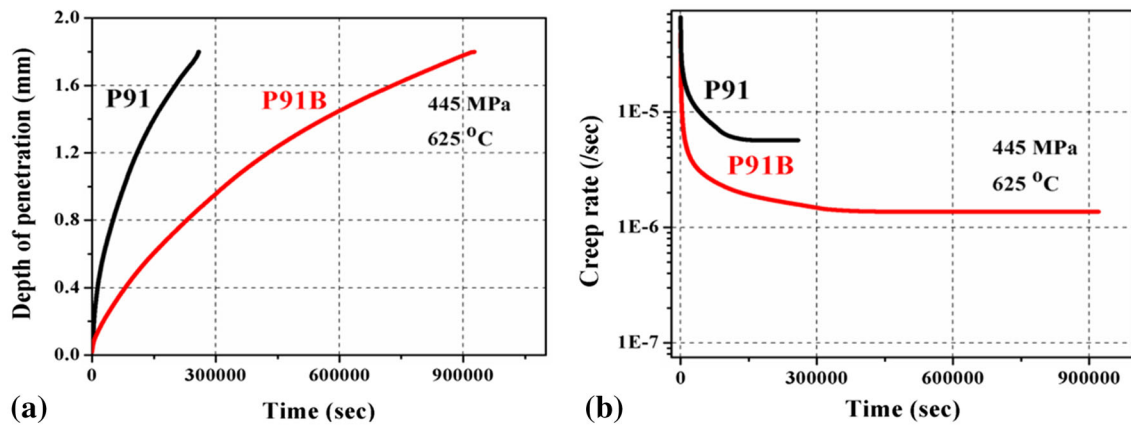
Fig. 5 (a) Depth of penetration vs. time plot-P91 and P91B and (b) impression velocity vs. time plot-P91 and P91B
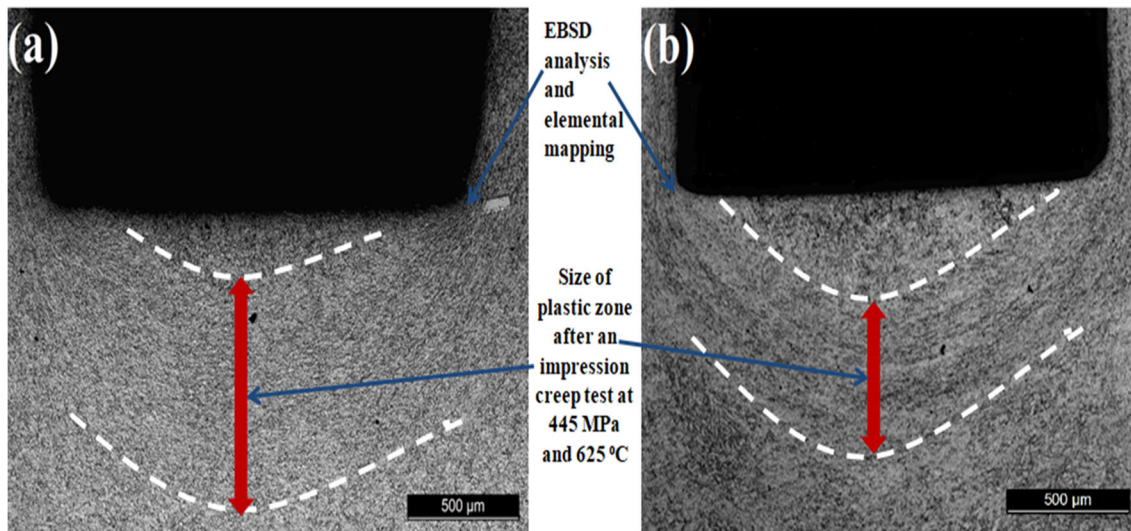

Fig. 6 Microstructural deformation at deformed plastic zones in impression-crept (IC) specimens (a) photomicrograph for IC-P91 and (b) photomicrograph for IC-P91B

boundaries. This infers that high energy is required to slide PAGs over each other in P91B since boron hinders coarsening of $M_{23}C_6$ carbides. Presence of fine carbides in microstructure is known to hinder dislocation motion as well as assure efficient grain boundary hardening in P91B.

Figure 3(b) shows the distribution of KAM values in terms of number fraction for both as-received alloys. Relatively large fraction of lower KAM values in P91B is due to effect of big martensite laths, whereas coarse carbides lead to a very large fraction of higher KAM values in P91. Generally for most polycrystalline metallic materials, the deformation mechanism is motion assisted by dislocations referred to as slip (Ref 41). Hence, phenomenon of slip becomes essential for understanding deformation behavior of metals. The easiness with which slip can occur within a polycrystalline material is calculated by Taylor factor ($\bar{M}$) by providing slip system and load axis in EBSD. Higher is $\bar{M}$ value, more difficult is to deform the material. Creep-strengthened alloys P91 and P91B have BCC type of crystal structure, and therefore preferred slip direction is a closed packed direction. The slip system and loading axis given for determining $\bar{M}$ value were $\{hkl\}\langle uvw\rangle$ $\{001\}\langle100\rangle$ and normal axis loading, i.e., rolled sheet, respectively.

Figure 2(g) and (h) shows Taylor factor maps for as-received P91 and P91B steels reflecting ease of slip for individual grain. Large variation in $\bar{M}$ values can be observed for P91 than its counterpart. It may be noted from Taylor factor charts of both alloys in Fig. 3(c) and (d) that relatively lower $\bar{M}$ values are obtained for boron-free P91 steel spread across the microstructure than boron-added P91 steel. Such observation is held responsible to size, shape and mobility of martensite laths which happen to be long, wide and less mobile in P91B than in P91 as shown by IPF maps and relatively large fraction of high $\bar{M}$ values in P91B. Also, low $\bar{M}$ values in PAGs of P91 indicate easy slip than in P91B.

From elemental maps of microalloying elements for P91 shown in Fig. 4(a) and (b), it is observed that chromium carbides are devoid of boron (assuming Cr exists in P91 as $M_{23}C_6$), non-uniformly distributed and are located in a long-range order segregating mainly toward lath boundaries. But in P91B, chromium carbides are fine, enriched with boron and are uniformly distributed across the iron matrix. This is deduced from relatively low percent concentration of chromium at those regions in the microstructure in P91B where the percent concentration of boron is moderately high as detected by WDS
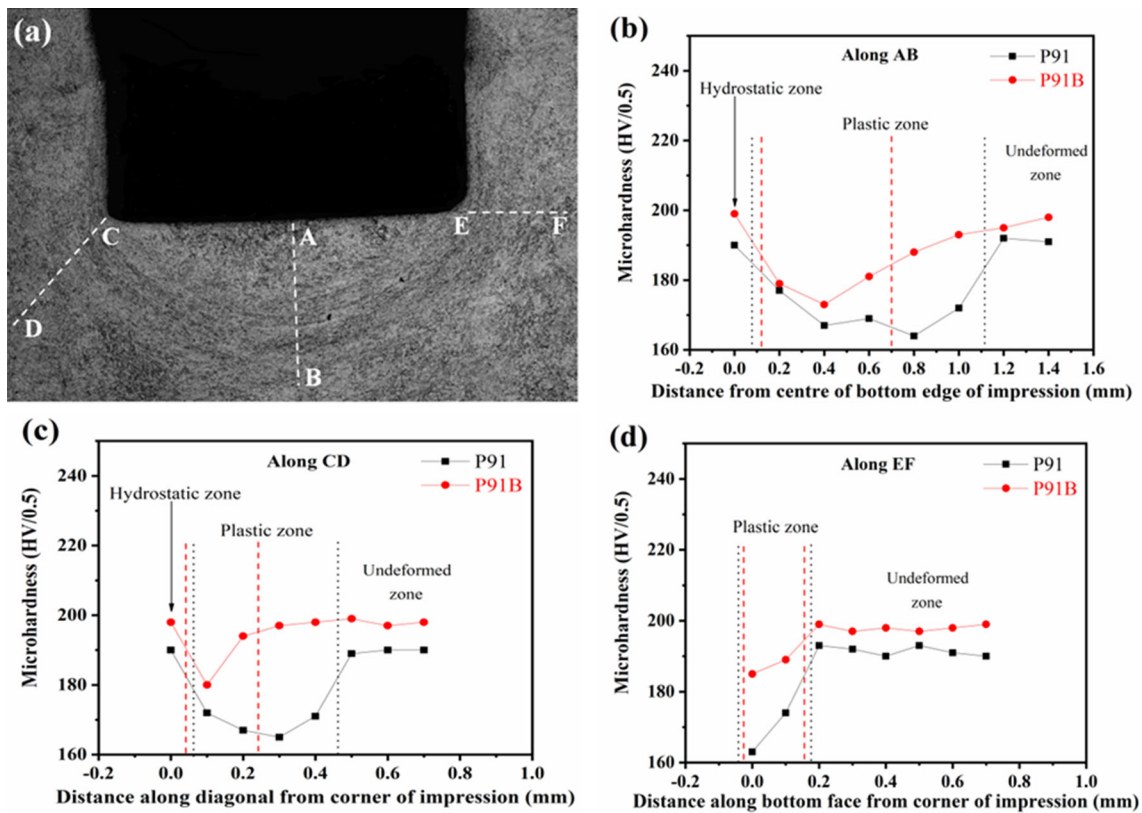
Fig. 7 Microhardness variation at deformed plastic zones in impression-crept (IC) specimens of P91 and P91B

area scans. Low carbon concentration in P91B signifies its fine distribution in carbide form than P91 where coarse carbides are present due to high carbon concentration. Interspacing for MX type of carbides of vanadium, molybdenum and niobium is less in P91B than in P91 where non-uniform spacing among these types of carbides forming elements is observed. Though molybdenum is known to provide solid solution strengthening in heat resistant steels, its fine precipitation with carbon compensates reduction in strengthening as the hardness for Mo_2C carbide overlaps with the hardness of $M_{23}C_6$ carbide (Ref 42).

EBSD and WDS analysis of as-received steels showed that the addition of 100-ppm boron in P91 alters the microstructure considerably. Major differences were observed in fraction of martensite lath boundaries being dominant in P91B, considerably higher KAM values at PAGBs of P91 than those of P91B, high values of Taylor factor in P91B than in P91, boron-rich $M_{23}C_6$ carbides and less interspacing among MX particles in P91B than in P91.

### 3.2 Impression Creep Curves for P91 and P91B Steels

Figure 5(a) gives the impression creep plots between depth of penetration and time for as-received P91 and P91B steels at 625 °C and 445 MPa. It may be noted that both creep tests were stopped at 1.8 mm depth of penetration (DOP). Time taken to reach this DOP is nearly ~ 72 h for P91, whereas P91B takes ~ 258 h, indicating 3.5 times fold increase in creep resistance to same punching stress and temperature during impression creep. However, this curve gives only primary and secondary creep stages, due to compressive nature of loading in an impression creep test. The creep rate versus time plot is

shown in Fig. 5(b). The primary creep stage which reflects an increase in resistance of metal due to strain hardening before it enters into true steady state is larger in P91B than in P91. The fine dispersion of $M_{23}C_6$ and MX carbides in iron matrix produces a most favorable microstructure which assists in retarding creep rate during transient creep period. MCR for P91 as found from creep rate versus time plot is of the order 5.67×10^{-6} per second which is relatively higher than 1.38×10^{-6} per second as obtained for P91B. This infers that P91 creeps faster and attains steady state earlier than P91B. The existence of fine carbides in P91B on grain boundaries combined with a bigger PAG size and strong martensitic lath structure as confirmed by microstructural studies gives increased resistance to penetration and thereby lowers MCR.

3.3 Characterization of Impression-Crept P91 and P91B Steel Specimens

3.3.1 Optical Microscopy and Microhardness at the Deformed Plastic Zone. Figure 6(a) and (b) shows local microstructural evolution obtained after high-temperature impression creep loading surrounding the indenter in P91 and P91B steels, respectively. The three zones are differentiated by broken white curved lines.

It may be noted that zone of hydrostatic stress is small in P91, but the deformed plastic zone with wide shear deformation is large in comparison with P91B. The size of plastic zone in P91 and P91B is 697 and 466 μm, respectively. This means relatively less plastic flow of metal takes place under the state of shear stress in P91B. Further, it signifies that the volume of interaction excluding the zone of hydrostatic stress during impression creep is dependent on creep resistance of the
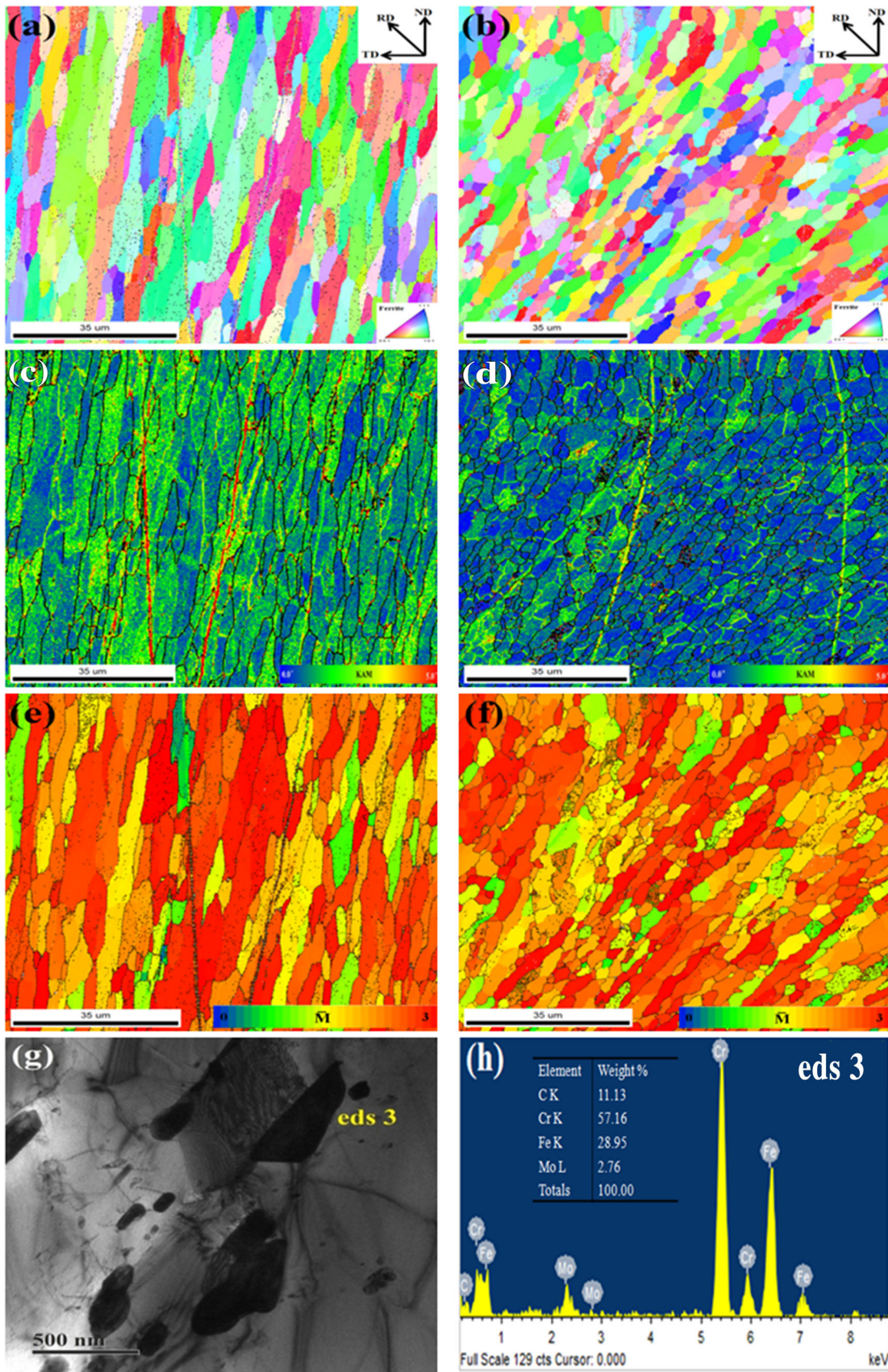
Fig. 8 EBSD color-coded maps of impression-crept specimens (a) P91-IPF map with grain boundaries, (c) P91-KAM map, (e) P91-Taylor factor, (b) P91B-IPF map with grain boundaries, (d) P91B-KAM map, (f) P91B-Taylor factor, (g) bright-field TEM-P91 crept and (h) spot EDS-P91 crept (Color figure online)
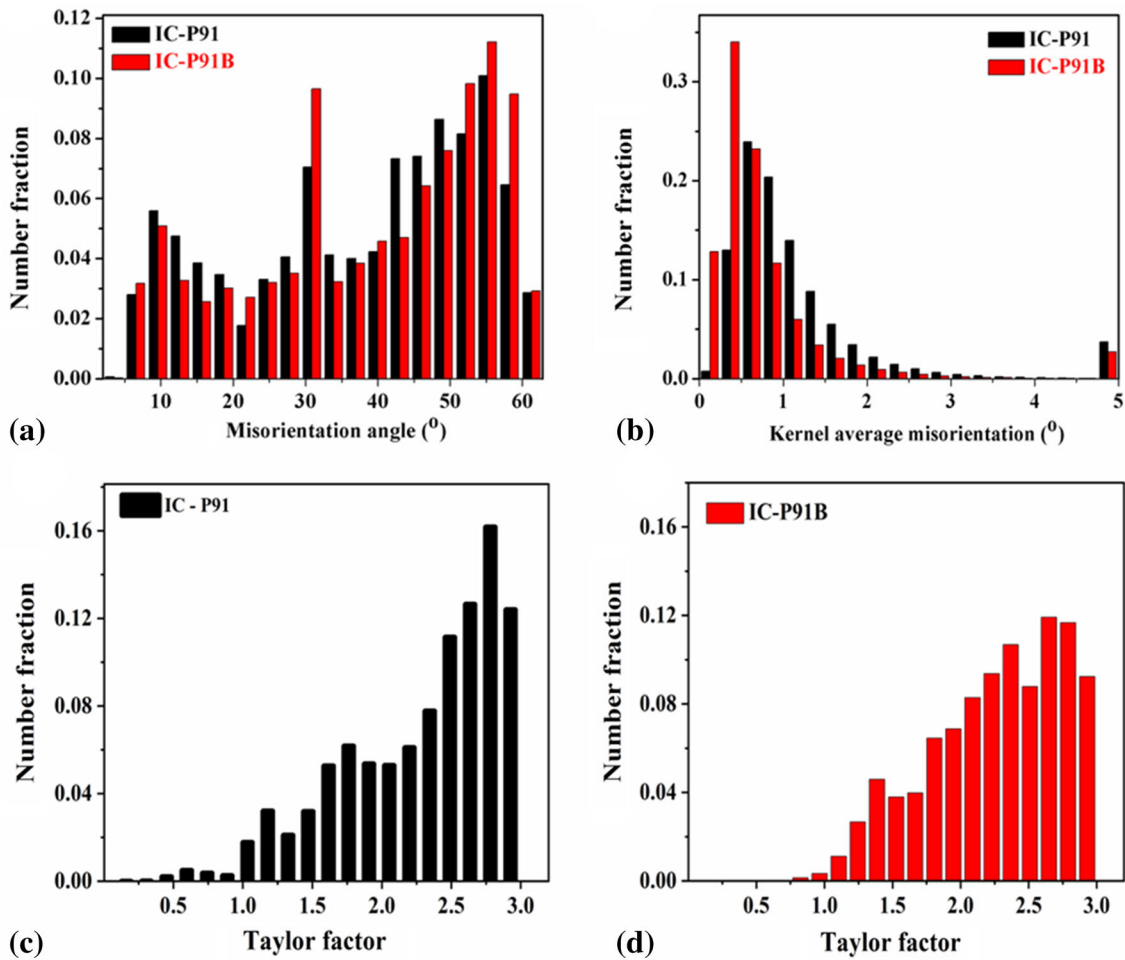
Fig. 9 EBSD analysis of impression-crept specimens (a) misorientation angle chart-P91 and P91B, (b) KAM chart-P91 and P91B, (c) P91-Taylor factor chart and (d) P91B-Taylor factor chart

Table 2 EBSD analyses of as-received steels and their impression-crept specimens

| Sample | Grain boundary fraction, % | | | |
	HAGB (Θ > 10°)	LAGB (Θ ∼ 2°–10°)	HAGB/LAGB ratio	KAM, °
AR-P91	71.2	28.8	2.47	1.39
P91-crept	52.6	47.4	1.10	1.16
AR-P91B	66.7	33.3	2.00	0.68
P91B-crept	70.9	29.1	2.43	0.77

material which happens to be small in boron-added P91. The zone of hydrostatic stress is subtracted since there is no effect of stress in this zone as shown by simulation studies earlier (Ref 43).

As-received P91 and P91B steels exhibited an average microhardness value of ∼ 244 HV/0.5 and ∼ 242 HV/0.5, respectively. To realize variation in microhardness across the deformed plastic zone for both alloys, hardness was taken at an interval of 'd × 3' where 'd' is the diagonal length of a microindentation in 'mm' as standardized by ASTM along broken lines marked in Fig. 7(a) (Ref 44). Measured values of microhardness were reconstructed in the form of graphs as shown in Fig. 7(b), (c) and (d). From hardness graphs, it can be

observed that for both impression-crept microstructures, a hardness drop of the order 40 HV/0.5-50 HV/0.5 at zone of hydrostatic stress and unaffected zone with no plastic deformation takes place in comparison with the as-received state. This is due to short-term aging of P91 and P91B steel specimens at 625 °C during which the impression creep test was carried out for 72 and 258 h, respectively (Ref 45). Naveena et al. observed a high hardness in the deformed plastic zone of impression-crept 316LN stainless steel (Ref 46). However, it is not observed at deformed plastic zones of impression-crept P91 and P91B steel samples. Rather hardness drop further increases at the deformed plastic zone than other zones and hardness drop being more and long in P91 owing to
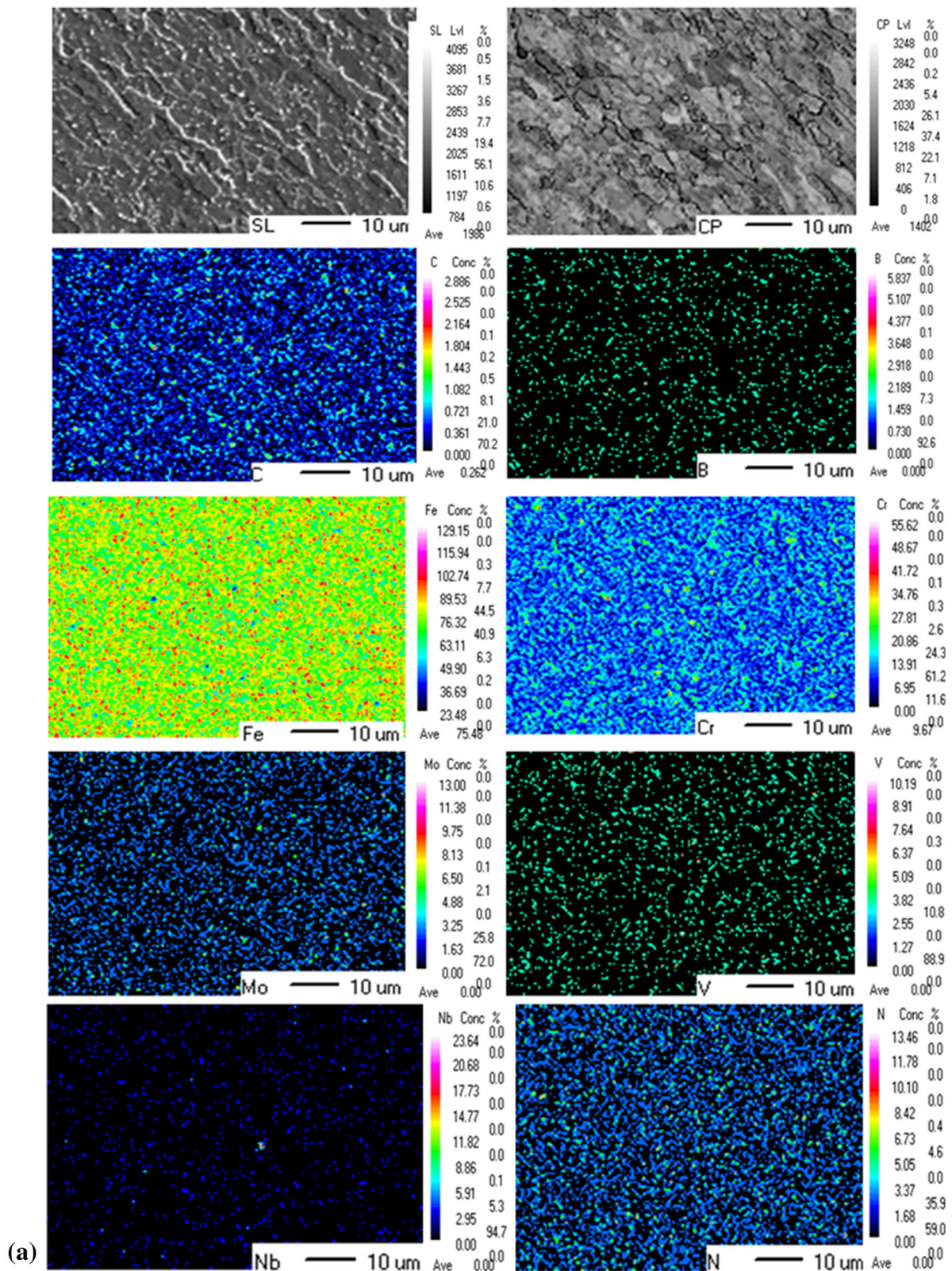
Fig. 10 Elemental mapping at crept deformed zone of steels (a) P91 and (b) P91B

bigger plastic zone. Since P91 is precipitate-hardened alloy, pronounced hardness drop in plastic zone indicates a reduction in solid solution strengthening which takes place due to the decrease in carbon availability in matrix solution in this zone and simultaneous coarsening of precipitates (Ref 47).

3.3.2 EBSD and WDS Analysis at the Deformed Plastic Zone. For analyzing the deformation behavior in impression-crept (IC) specimens, EBSD and WDS area scans were captured at corners of impression since the plastic zone begins
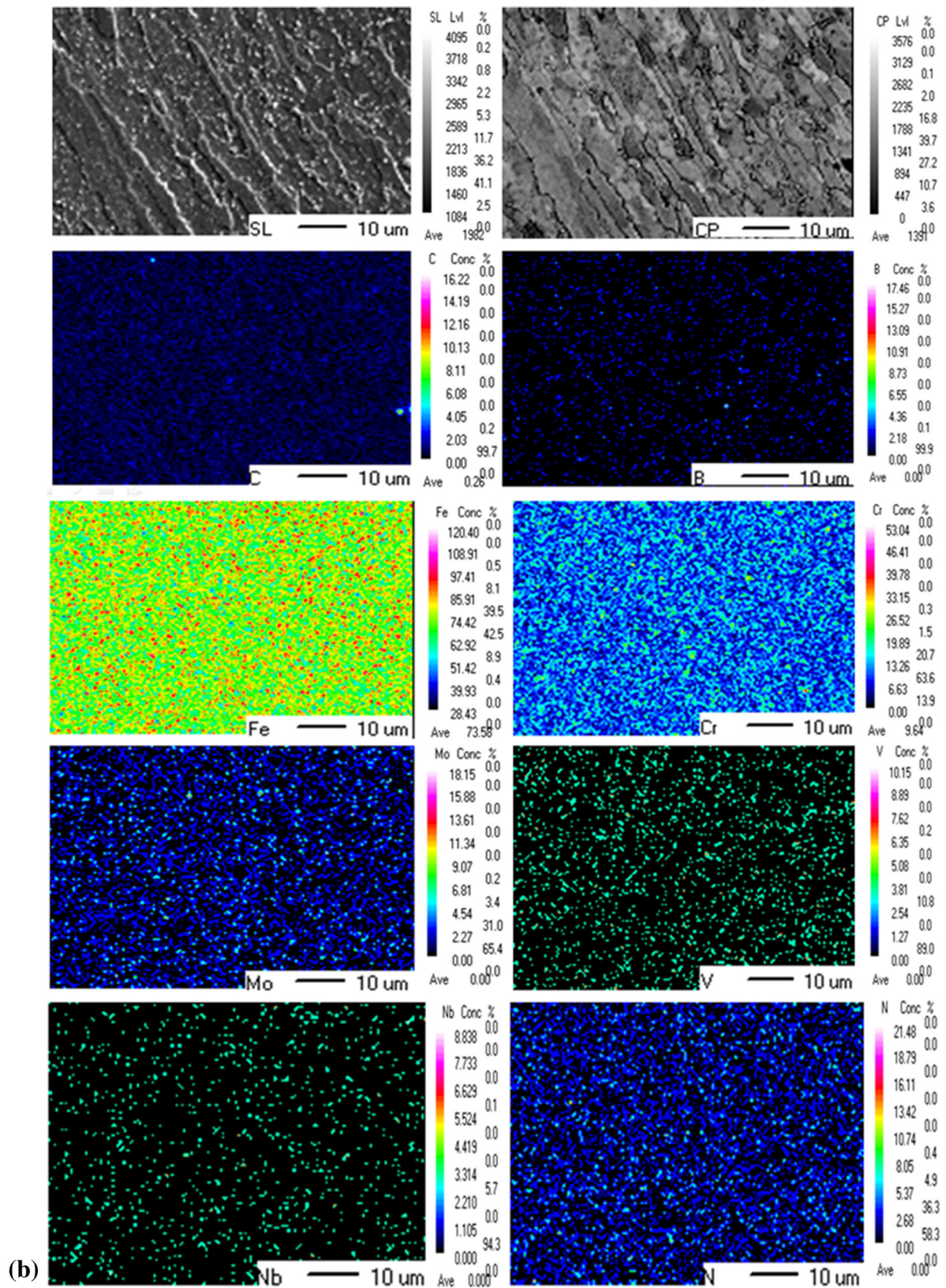
Fig. 10 continued

to develop from boundaries of indentation and therefore density of plastic deformation lines is highest at these locations (Ref 43). Color-coded maps of deformed IC specimens are shown in

Fig. 8, and EBSD statistical charts obtained at same inputs for as-received steels are presented in Fig. 9. Comparisons of EBSD analyzed data before and after impression creep tests are

given in Table 2. IPF maps showing deformed grains of impression-crept specimens taken from locations as indicated in Fig. 6(a) and (b) are shown in Fig. 8(a) and (b). It is observed that elongated grains are dominant in P91 and percent fraction of LAGBs increase after impression creep test as tabulated for P91. On the other hand, plastic flow of grains is seen in P91B and a decrease in percent fraction of LAGBs. Therefore, ratio of HAGB/LAGB increases for P91B after impression creep in contrast to P91. Such nucleation and growth of small strain-free grains along with elongated grains during impression creep deformation in boron-added P91 steel can be attributed to dynamic recrystallization (Ref 48). Newly formed grains are not able to merge with large grains during creep loading due to the presence of solute elements combined with fine carbides on grain boundaries which hold back the movement of dislocations across them. It may be observed from Fig. 8(c) and 9(b) that a relatively big fraction of higher KAM values exist in P91 which indicates extensive strain hardening of the microstructure leading to the formation of recovered grains with respect to the deformed state. This further implies that dislocations should be arranged in the recovered state in P91, since no effective hindrance to their movement was present during creep loading and it led to an increase in deformed plastic zone with wide shear deformation. This is affirmed by $M_{23}C_6$ carbide coarsening in plastic zone of P91 as shown in Fig. 8(g) in which percentage of carbon and chromium increases considerably after impression creep as regards as-received state.

Also, a higher fraction of $\bar{M}$ values after creep test in the deformed plastic zone of impression-crept P91 than P91B as shown in Fig. 8(e) and 9(c) signify no exposure to fresh orientations for further deformation, thus approving strain-hardened microstructure. Less fraction of higher KAM values as observed in Fig. 8(d) and 9(b) reflects defect-free regions at deformed plastic zone of P91B impression-crept specimen. This means that no recovery of PAGs took place in P91B and a higher driving force was toward recrystallization. Further, it suggests that boron pinning to dislocations is effective in P91B which strengthens grain boundaries and lowers MCR. Lower fraction of $\bar{M}$ values as noted in Fig. 8(f) and 9(d) after impression creep in P91B implies that new orientations have been exposed and deformed microstructure is still available to take deformation.

Elemental maps of impression-crept P91 in Fig. 10(a) confirm $M_{23}C_6$ carbide coarsening since the carbon concentration drops at deformed plastic zone which has been confirmed by drop in microhardness too. This infers that 22-ppm boron in P91 fails to delay coarsening of $M_{23}C_6$ carbides, thus reducing pinning force of carbides against sliding of grain boundaries during impression creep. Hence, P91 shows poor creep performance than P91B where a relatively high concentration of carbon in iron matrix is observed at the deformed plastic zone as detected by WDS and shown in Fig. 10(b). This is attributed to 100-ppm boron in P91B steel which delays the coarsening of $M_{23}C_6$ carbides, and subsequently these carbides are effective in providing pinning force for obstructing grain sliding. Therefore, P91B shows better creep performance at 625 °C and 445 MPa.

Nonetheless, no significant differences are observed in the concentrations of vanadium, niobium and nitrogen after impression creep. However, molybdenum is uniformly distributed in impression-crept P91B, indicating well-dispersed Mo_2C-type carbide which could also be held responsible for enhancing creep strength at elevated temperatures and high stress in this steel alloy.

4. Conclusions

To understand the role of boron on creep deformation behavior in P91 steel, impression creep tests were conducted on P91 and P91B steels. Based on microstructural analysis of as-received steels and impression-crept specimens of P91 and P91B steels, the following conclusions are drawn:

1. Addition of 100-ppm boron in P91 steel alters the microstructure considerably. Characterization of as-received steels by OM, TEM and WDS revealed a bigger PAG size with acicular shape, less inter-lath spacing, presence of small precipitates and less inter-particle distance in P91B than in P91. EBSD analysis showed that an enhancement in fraction of martensite lath boundary, decline in fraction of low-angle grain boundaries, reduction in local strain on prior austenite grain boundaries and less lath mobility in P91B result in an enhanced martensitic lath structure in contrast to P91.
2. P91B steel is 3.5 times resistant than P91 steel to a punching stress of 445 MPa at 625 °C during an impression creep test. The fine dispersion of $M_{23}C_6$ carbides in martensite produces a most favorable microstructure which retards creep rate during transient creep period in P91B. The existence of fine carbides on grain boundaries combined with bigger PAG size and strong martensitic lath structure gives increased resistance to penetration and thereby lowers MCR in P91B.
3. Impression creep technique is found sensitive to addition of boron in precipitate-hardened P91 steel alloy. Microstructure in P91 strain hardens with extensive precipitate coarsening under a state of high-stress and high-temperature creep exposure leading to an increased size of deformed plastic zone, whereas dynamic recrystallization leads to formation of strain-free grains with negligible precipitate coarsening in P91B which contribute to improved creep performance.
4. Results also indicate an increase in HAGB/LAGB ratio in P91B after impression creep in plastic zone which explains the role of boron in retarding formation of small angle grain boundaries which are held responsible for easy propagation of intergranular cracking at outer heat-affected zone of P91 weldments leading to type IV cracking.

References

1. J. Wheeldon, J. Parkes, and D. Dillon, UltraGen: A Proposed Initiative by EPRI to Advance Deployment of Ultra Supercritical Pulverized Coal Power Plant Technology with Near Zero Emissions and CO_2 Capture and Storage, in *Proceedings of 5th International Conference on Advanced Materials Technology for Fossil Power Plants*, 2007

2. R.L. Klueh, Ferritic/Martensitic Steels for Advanced Nuclear Reactors, *Trans. Indian Inst. Met.*, 2009, **62**(2), p 81–87

3. S.K. Albert, M. Tabuchi, H. Hongo, T. Watanabe, K. Kubo, and M. Matsui, Effect of Welding Process and Groove Angle on Type IV Cracking Behaviour of Weld Joints of a Ferritic Steel, *Sci. Technol. Weld. Join.*, 2005, **10**(2), p 149–157

4. Y. Wang and L. Li, Microstructure Evolution of Fine Grained Heat Affected Zone in Type IV Failure of P91 welds, *Weld. J*, 2016, **95**, p 27–36

5. J. Baral, J. Swaminathan, and R.N. Ghosh, Creep Behaviour of 9CrMoNbV (P91) Steel Having a Small Amount of Boron, *Procedia Eng.*, 2013, **55**, p 88–92

6. F. Abe, M. Tabuchi, M. Kondo, and S. Tsukamoto, Suppression of Type IV Fracture and Improvement of Creep Strength of 9Cr Steel Welded Joints by Boron Addition, *Int. J. Press. Vessels Pip.*, 2007, **84**(1), p 44–52

7. F. Abe, M. Tabuchi, S. Tsukamoto, and T. Shirane, Microstructure Evolution in HAZ and Suppression of Type IV Fracture in Advanced Ferritic Power Plant Steels, *Int. J. Press. Vessels Pip.*, 2010, **87**(11), p 598–604

8. M. Kondo, M. Tabuchi, S. Tsukamoto, F. Yin, and F. Abe, Suppressing Type IV Failure via Modification of Heat Affected Zone Microstructures Using High Boron Content in 9Cr Heat Resistant Steel Welded Joints, *Sci. Technol. Weld. Join.*, 2006, **11**(2), p 216–223

9. F. Yang and J.C. Li, Impression Test: A Review, *Mater. Sci. Eng. R*, 2013, **74**(8), p 233–253

10. J.C. Li, Impression Creep and Other Localized Tests, *Mater. Sci. Eng. A*, 2002, **322**(1), p 23–42

11. N.D. Vijayanand, V. Ganesan, K. Laha, and M.D. Mathew, Evaluation of Creep Deformation Behaviour of Different Microstuctural Zones of 316LN SS Weld Joint Using Impression Creep Testing Technique, *Mater. Sci. Technol.*, 2014, **30**(10), p 1223–1228

12. N.D. Vijayanand, V. Ganesan, K. Laha, and M.D. Mathew, Evaluation of the Effect of Nitrogen on Creep Properties of 316LN Stainless Steel from Impression Creep Tests, *Mater. Sci. Eng. A*, 2012, **552**, p 112–118

13. M.D. Mathew and D. Vijayanand, Impression Creep Behaviour of 316LN Stainless Steel, *J. Mater. Eng. Perform.*, 2013, **22**(2), p 492–497

14. T. Hasegawa, Y.R. Abe, Y. Tomita, N. Maruyama, and M. Sugiyama, Microstructural Evolution During Creep Test in 9Cr–2W–V–Ta Steels and 9Cr–1Mo–V–Nb Steels, *ISIJ Int.*, 2001, **41**(8), p 922–929

15. C. Pandey, M.M. Mahapatra, P. Kumar, R.S. Vidyrathy, and A. Srivastava, Microstructure-Based Assessment of Creep Rupture Behaviour of Cast-Forged P91 Steel, *Mater. Sci. Eng. A*, 2017, **695**, p 291–301

16. K. Maruyama, K. Sawada, and J.I. Koike, Strengthening Mechanisms of Creep Resistant Tempered Martensitic Steel, *ISIJ Int.*, 2001, **41**(6), p 641–653

17. Y.Z. Shen, S.H. Kim, C.H. Han, H.D. Cho, and W.S. Ryu, TEM Investigations of MN Nitride Phases in a 9% Chromium Ferritic/Martensitic Steel with Normalization Conditions for Nuclear Reactors, *J. Nucl. Mater.*, 2009, **384**(1), p 48–55

18. Y.Z. Shen, S.H. Kim, C.H. Han, H.D. Cho, W.S. Ryu, and C.B. Lee, Vanadium Nitride Precipitate Phase in a 9% Chromium Steel for Nuclear Power Plant Applications, *J. Nucl. Mater.*, 2008, **374**(3), p 403–412

19. Y.Z. Shen, S.H. Kim, H.D. Cho, C.H. Han, and W.S. Ryu, Precipitate Phases of a Ferritic/Martensitic 9% Cr Steel for Nuclear Power Reactors, *Nucl. Eng. Des.*, 2009, **239**(4), p 648–654

20. N.Z. Gutierrez, H. De Cicco, J. Marrero, C.A. Danón, and M.I. Luppo, Evolution of Precipitated Phases During Prolonged Tempering in a 9%Cr1%MoVNb Ferritic–Martensitic Steel: Influence on Creep Performance, *Mater. Sci. Eng. A*, 2011, **528**(12), p 4019–4029

21. F. Abe, M. Tabuchi, and S. Tsukamoto, Alloy Design of Martensitic 9Cr-Boron Steel for a USC Boiler at 650 °C—Beyond Grades 91, 92 and 122, in *Energy Materials,* Springer, Cham, 2014, p. 129–136

22. H.Y. Yu and J.C.M. Li, Computer Simulation of Impression Creep by the Finite Element Method, *J. Mater. Sci.*, 1977, **12**(11), p 2214–2222

23. T.H. Hyde, K.A. Yehia, and A.A. Becker, Application of the Reference Stress Method for Interpreting Impression Creep Test Data, *Mater. High Temp.*, 1995, **13**(3), p 133–138

24. G. Nayyeri and R. Mahmudi, The Microstructure and Impression Creep Behaviour of Cast, Mg–5Sn–xCa Alloys, *Mater. Sci. Eng. A*, 2010, **527**(7–8), p 2087–2098

25. P.S. Godavarti and K.L. Murty, Creep Anisotropy of Zinc Using Impression Tests, *J. Mater. Sci. Lett.*, 1987, **6**(4), p 456–458

26. L. Peng, F. Yang, J.F. Nie, and J.C.M. Li, Impression Creep of a Mg-8Zn-4Al-0.5Ca Alloy, *Mater. Sci. Eng. A*, 2005, **410**, p 42–47

27. D. Dorner, K. Röller, B. Skrotzki, B. Stöckhert, and G. Eggeler, Creep of a TiAl Alloy: A Comparison of Indentation and Tensile Testing, *Mater. Sci. Eng. A*, 2003, **357**(1–2), p 346–354

28. D. Chiang and J.C.M. Li, Impression Creep of Lead, *J. Mater. Res.*, 1994, **9**(4), p 903–908

29. S.N.G. Chu and J.C.M. Li, Impression Creep of β-Tin Single Crystals, *Mater. Sci. Eng. A*, 1979, **39**(1), p 1–10

30. S.N.G. Chu and J.C.M. Li, Impression Creep: A New Creep Test, *J. Mater. Sci.*, 1977, **12**(11), p 2200–2208

31. J. Hald, Creep Strength and Ductility of 9 to 12% Chromium Steels, *Mater. High Temp.*, 2004, **21**(1), p 41–46

32. D. Jandová and J. Kasl, Influence of Precipitation on Dislocation Substructure and Creep Properties of P91 Steel Weld Joints, *Mater. High Temp.*, 2010, **27**(2), p 135–140

33. Y. Zhang, Changes in Microstructure and Mechanical Properties of P91 Weld Metal During Creep. PhD thesis, University of Nottingham, 2009, p. 145–150

34. C.G. Panait, W. Bendick, A. Fuchsmann, A.F.G. Lorenzon, and J. Besson, Study of the Microstructure of the Grade 91 Steel After More Than 100,000 h of Creep Exposure at 600 °C, *Int. J. Press. Vessels Pip.*, 2010, **87**(6), p 326–335

35. D.T. Erten, T.T. Nguyen, T.M. Jeong, and K.B. Yoon, Creep Deformation and Rupture Behaviour of Service Exposed P91 Weld and Base Steel Measured by Miniature Tensile Creep Testing, *Mater. High Temp.*, 2017, **34**(5–9), p 425–433

36. F.H. Lege, *ASM Hand Book, Metallography and Microstructures*, Vol 9, American Society for Metals, Cleveland, 1984, p 605

37. I. Fedorova, A. Kostka, E. Tkachev, A. Belyakov, and R. Kaibyshev, Tempering Behavior of a Low Nitrogen Boron-Added 9% Cr Steel, *Mater. Sci. Eng. A*, 2016, **662**, p 443–455

38. K. Sawada, K. Kubo, and F. Abe, Creep Behaviour and Stability of MX Precipitates at High Temperature in 9Cr-0.5Mo-1.8W-V Nb Steel, *Mater. Sci. Eng. A*, 2001, **319**, p 784–787

39. B. Sonderegger, S. Mitsche, and H. Cerjak, Microstructural Analysis on a Creep Resistant Martensitic 9–12% Cr Steel Using the EBSD Method, *Mater. Sci. Eng. A*, 2008, **481**, p 466–470

40. B. Sonderegger, S. Mitsche, and H. Cerjak, Martensite Laths in Creep Resistant Martensitic 9–12% Cr Steels—Calculation and Measurement of Misorientations, *Mater. Charact.*, 2007, **58**(10), p 874–882

41. G.E. Dieter, *Mechanical Metallurgy*, 2nd ed., McGraw-hill, Maidenhead, 1988, p 90–99

42. M. Akhtar, Metallurgical Characterisation of Simulated Heat Affected Zone in Boron Modified P91 Steel. Master's Thesis, NIT, Warangal, 2017, p. 22–23. https://doi.org/10.13140/rg.2.2.12593.68967

43. G. Kumar and M.D. Mathew, Finite Element Analysis of Plastic Deformation During Impression Creep, *J. Mater. Eng. Perform.*, 2015, **24**(4), p 1741–1753

44. ASTM, *Standard Test Method for Microhardness of Materials, Annual Book of ASTM Standards, Part 14*, 1999

45. V. Sklenicka, K. Kucharova, M. Svobodova, P. Kral, M. Kvapilova, and J. Dvorak, The Effect of a Prior Short-Term Ageing on Mechanical and Creep Properties of P92 Steel, *Mater. Charact.*, 2018, **136**, p 388–397

46. V. Naveena, P. Shankar, and M.D.Mathew Parameswaran, Impression Creep Deformation Behaviour of 316LN Stainless Steel, *Mater. High Temp.*, 2015, **32**(6), p 583–591

47. C. Pandey, M.M. Mahapatra, P. Kumar, N. Saini, and J.G. Thakre, Nano-size Particle Evolution During Heat Treatment of P91 Steel and Their Effect on Micro Hardness, *Trans. Indian Inst. Met.*, 2017, p. 1–8

48. K. Huang and R.E. Logé, A Review on Dynamic Recrystallization Phenomena in Metallic Materials, *Mater. Des.*, 2016, **111**, p 548–574